Histidine 73 methylation coordinates β-actin plasticity in response to key environmental factors

Adrien Schahl[1,2], Louis Lagardere[2], Brandon Walker[3], Pengyu Ren[3], Hugo Wioland[4], Maya Ballet[4], Antoine Jégou[4], Matthieu Chavent[1,5,*], Jean-Philip Piquemal[2,*]

***For correspondence:** matthieu.chavent@univ-tlse3.fr, jean-philip.piquemal@sorbonne-universite.fr ( )

[1]Institut de Pharmacologie et de Biologie Structurale, Université de Toulouse, CNRS, Université Paul Sabatier, 31400 Toulouse, France; [2]Sorbonne Université, LCT, UMR 7616 CNRS, F-75005, Paris, France; [3]Department of Biomedical Engineering, The University of Texas at Austin, Austin, Texas 78712, United States; [4]Université Paris Cité, CNRS, Institut Jacques Monod, F-75013 Paris, France; [5]Laboratoire de Microbiologie et Génétique Moléculaires (LMGM), Centre de Biologie Intégrative (CBI), Université de Toulouse, CNRS, UPS, France

Abstract Although β-actin is one of only two ubiquitously expressed actin isoforms present in all cells, it remains understudied biochemically due to technical challenges associated with protein production and purification. In particular the importance of histidine 73 (H73) methylation of β-actin remains unclear. Here, we employed molecular dynamics simulations using an advanced method that couples a polarizable force field to large scale adaptive sampling to achieve higher level of interatomic interaction accuracy when compared to classical atomic force fields. This methodology enabled us to investigate the effect of H73 methylation on the plasticity of both β-actin monomers (G-actin) and filaments (F-actin) and capture how subtle conformational changes are relevant to β-actin function. We uncovered that H73 methylation enhances the opening of the nucleotide binding cleft and modifies allosteric paths linking subdomains 2 and 4 (SD2 and SD4) of actin. We showed that in F-actin H73 methylation affects the opening of a backdoor and limits the release of the inorganic phosphate, as confirmed by biochemical assays. We also observed that effects of H73 methylation are modulated by the type of nucleotide bound in the actin cavity and ions surrounding the protein. Taken together, these results shed new light onto how H73 methylation regulates β-actin plasticity and coordinates impact of several key environmental factors.

Introduction

The actin cytoskeleton is involved in numerous cellular functions, such as cell shape maintenance, proliferation, and migration ***Svitkina*** (***2018***). Over many decades, studies using α-actin, the main actin isoform present in skeletal muscle tissue ***Perrin and Ervasti*** (***2010***); ***Varland et al.*** (***2019***) as a model of choice, revealed that actin undergoes large conformational changes as it executes its function ***Merino et al.*** (***2020***). Thus, it is well established that actin monomers assemble to nucleate and elongate filaments ***Wegner*** (***1982***), which form the basis of the cytoskeleton. Structurally, addition of actin monomers at filament ends induces a transition from the globular actin monomer (G-actin) to a flattened F-actin structure ***Oda et al.*** (***2009***). In the filament, the actin structural plastic-

ity is also important for its ATPase activity, which requires a high level of plasticity. Actin molecules achieve this plasticity through movement of its four distinct subdomains (SD1-4) that change relative orientations in response to nucleotide binding, ATP hydrolysis, and inorganic phosphate (Pi) release ***Blanchoin and Pollard*** (***2002***). These events, in turn, modulate the mechanical properties of the filament and interactions with many actin binding proteins ***Oosterheert et al.*** (***2023***).

In addition to being modulated by ATP and ADP binding ***Merino et al.*** (***2020***); ***Varland et al.*** (***2019***); ***Reynolds et al.*** (***2022***), and ATP hydrolysis, actin plasticity also depends on other environmental factors, such as the surrounding ions ***Kang et al.*** (***2012***). Furthermore, recent work has highlighted the importance of the methylation of histidine 73 (H73) in affecting filament formation and the rate of ATP hydrolysis in the monomeric form***Wilkinson et al.*** (***2019***). Although first reported more than six decades ago ***Johnson et al.*** (***1967***), H73 methylation has remained a biochemical oddity and continues to be somewhat of a functional mystery. Recent identification of SETD3 as the methyltransferase responsible for catalyzing this rare and rarely studied post-translational modification***Wilkinson et al.*** (***2019***); ***Kwiatkowski et al.*** (***2018***) has reignited interest in the role of H73 methylation in actin biology. Previous structural studies showed that H73 is located within a region of actin known as sensor loop (Fig 1-A) ***Graceffa and Dominguez*** (***2003***). Given this location, and the specific interactions methylated H73 makes with the nucleotide binding cleft located between subdomains 2 and 4 (SD2 and SD4; Fig 1-A), this PTM was proposed to be a key regulator that couples ATP hydrolysis and Pi release with filament formation***Nyman et al.*** (***2002***). However, many details of mechanism(s) that are governed by methylation of H73 in actin remain unknown. Additionally, the precise role of H73 methylation in actin dynamics and plasticity remains incompletely understood.

Here, we address some of these mechanistic questions using β-actin as a model system. We chose to focus on β-actin because it remains far less studied actin isoform, despite functional relevance. Firstly, unlike α-actin, which is only expressed in skeletal muscles, β-actin is ubiquitously expressed in all cells as a highly abundant housekeeping gene. Furthermore, β-actin plays a key role in early embryonic development, cell migration and growth ***Bunnell et al.*** (***2011***). More recently, β-actin has been shown to participate in chromatin remodeling ***Mahmood et al.*** (***2021***), and there is accumulating evidence that β-actin is important for epithelial-to-mesenchymal transition ***Dugina et al.*** (***2021***); ***Nietmann et al.*** (***2023***) and of interest in cancer research ***Guo et al.*** (***2013***). However, β-actin remains less studied than the α isoform, especially in terms of its biochemical mechanism and dynamics. This is primarily due to the fact that obtaining high-quality sample for in vitro studies has been a major hurdle for the field, until very recently ***Ceron et al.*** (***2022***); ***Hatano et al.*** (***2020***).

Over the last two decades, MD simulations have become an increasingly popular strategy for studying biological systems at different scales ***Vanommeslaeghe et al.*** (***2010***); ***Maier et al.*** (***2015***); ***Souza et al.*** (***2021***); ***Kim and Hummer*** (***2008***); ***Chu and Voth*** (***2005***). Notably, this methodology has been extensively employed to delineate various properties of actin, such as structural differences between nucleotide states ***Splettstoesser et al.*** (***2009***); ***Saunders et al.*** (***2014***); ***Jepsen and Sept*** (***2020***), the localization of water molecules in the actin binding site and their impact on protein plasticity and enzymatic properties ***Saunders and Voth*** (***2011***); ***McCullagh et al.*** (***2014***), interactions with small molecules ***Rennebaum and Caflisch*** (***2012***); ***Helal et al.*** (***2013***) and the dynamic behavior of filaments in diverse environments ***Chu and Voth*** (***2005***); ***Splettstoesser et al.*** (***2011***); ***Zsolnay et al.*** (***2020***); ***Schroer et al.*** (***2020***); ***Shamloo and Mehrafrooz*** (***2018***); ***Jaswandkar et al.*** (***2021***); ***Horan et al.*** (***2020***); ***Castaneda et al.*** (***2019***); ***Oosterheert et al.*** (***2023***). However, these computational studies almost exclusively focused on α-actin, while the β-actin isoform remains understudied, limiting our understanding of its unique dynamics and functional implications.

Even if MD simulations have been instrumental in the understanding of how ion and water molecules interact with proteins ***Song et al.*** (***2013***); ***Kopec et al.*** (***2018***); ***Bellissent-Funel et al.*** (***2016***); ***Hocky et al.*** (***2016***) the precise parametrization of these components is still challenging and depends on the system studied ***Kadaoluwa Pathirannahalage et al.*** (***2021***). Recent methodological

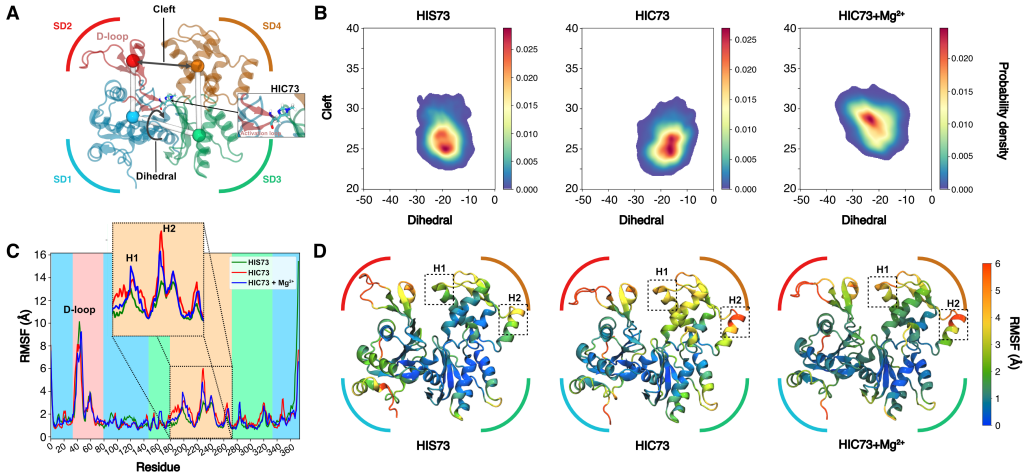

Figure 1. ATP-bound β-actin plasticity. A- Actin is divided in four subdomains: SD1 (blue), SD2 (red), SD3 (green), and SD4 (tan). The nucleotide-binding cleft (Cleft) represents the distance between SD2 and SD4 domains while the dihedral angle is formed by the four subdomains in the order SD2-SD1-SD3-SD4. The actin is represented with SD2 in upper left and SD4 in upper right (which corresponds to the back of the classic view of actin) to emphasize the positioning of Histidine 73. **B-** Distribution of cleft-dihedrals for actin without methylation (HIS73), or with methylation (HIC73) in presence of KCl and $MgCl_2$ (HIC73+Mg^{2+}). **C-** RMSF of each system. Zoom on the SD4 subdomain, with a focus on helix H1 (residues 200-206) and helix H2 (residues 228-232). Background colors correspond to subdomains presented in (A). **D-** Representation of each system colored according to their RMSF. Differences observed between HIS73, HIC73, and HIC+Mg^{2+} systems are all significant (Table S3).

developments on polarizable force-fields have drastically increased the accuracy of interactions between these molecules and proteins ***Shi et al.*** (***2015***); ***Melcr and Piquemal*** (***2019***); ***Jing et al.*** (***2019***, 2021); ***Lynch et al.*** (***2021***); ***El Ahdab et al.*** (***2021***); ***Célerse et al.*** (***2019***); ***Kratochvil et al.*** (***2016***); ***Li et al.*** (***2015***); ***El Khoury et al.*** (***2022***). In addition, the use of enhanced sampling methods allows exploring diverse unknown states hard to reach through the use of classical molecular dynamics simulations ***Jaffrelot Inizan et al.*** (***2021***); ***Bowman et al.*** (***2010***); ***Miao et al.*** (***2015***); ***Célerse et al.*** (***2022***); ***Ma et al.*** (***2023***).

Here, we employed MD simulation strategies that overcome the limitations of classical approaches by combining adaptive sampling with the AMOEBA polarizable force field to more accurately model interatomic interactions. We applied them to address outstanding challenges and provide new insights into β-actin biochemistry and how H73 methylation together with key environmental factors (ions and nucleotides), affect its dynamics and plasticity both in its core and extremities. This work sheds new light onto the plasticity of the β-actin isoform, where subtle structural changes can impact actin function, from the monomer to the filament.

Results

Histidine 73 methylation modulates the plasticity of ATP bound G-actin. We performed 1.52 µs long adaptive sampling polarizable molecular dynamics simulations for both α- and β-actin isoforms containing ATP bound nucleotide and magnesium ion in the active site, in the presence of 150 mM of KCl in solution. To assess the effect of H73 methylation on the G-actin dynamics, we simulated both non-methylated histidine (HIS73) and methylated histidine (HIC73) and measured the dihedral angle formed by the four subdomains, as well as the distance between SD2 and SD4 which defines the size of the nucleotide binding cleft (***Saunders et al., 2014***) (hereafter referred as "cleft") (Fig. 1A). For HIS73 β-actin, the protein fluctuated around a dihedral angle of c.a. -20° and a cleft size of 25 Å (Fig. 1B). The region of high density extends up to 27 Å indicating the capacity of the protein to widen the cleft during the course of the simulation (Fig. S1 and Movie S1). Remark-

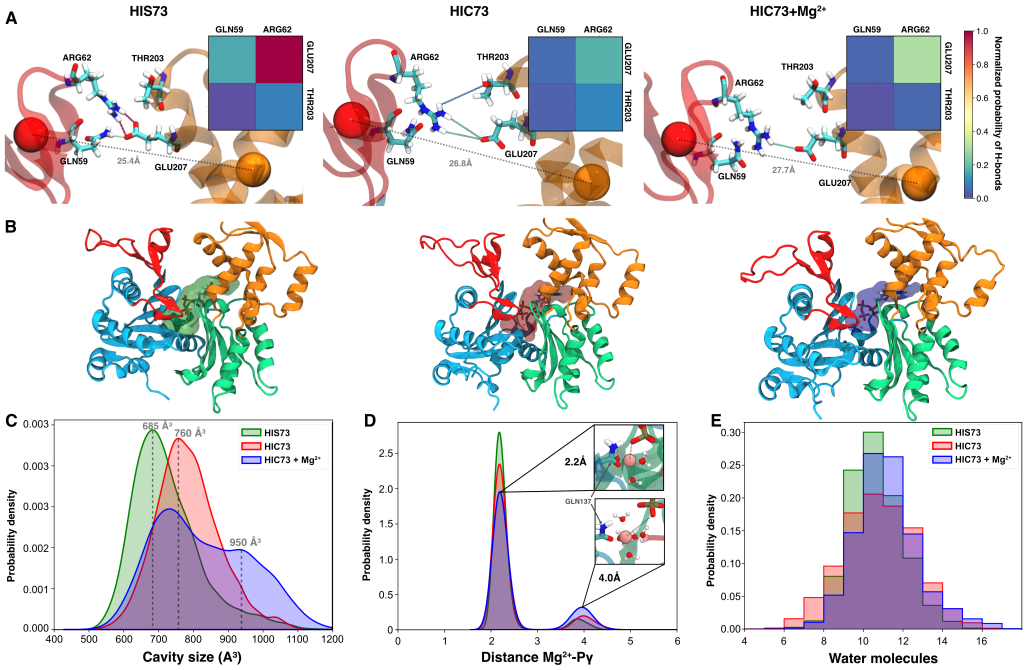

Figure 2. Role of methylation and magnesium ions on ATP-bound β-actin intrinsic flexibility. A- Representation of main residues interactions at the interface of SD2 and SD4. Interactions are colored in function of the normalized probability of hydrogen bonds between these residues during the simulations. **B-** Volume of the actin active for the most probable actin configurations presented in Figure 1-B. **C-** Distribution of the active site volume for each system presented in (B). **D-** Distribution of the distance between magnesium ion and γ-phosphate. **E-** Histograms of the number of water molecules around the magnesium ($\leq$ 5 Å) in the active site. The differences for the cavity volume and distance between magnesium ion and γ-phosphate observed between HIS73, and HIC73 and HIC+Mg^{2+} systems are significant (Table S3). The number of water molecule is not significantly different between these three systems (Table S3).

ably, despite differing from HIS73 slightly (presence of an additional -CH3 group), HIC73 induced notable changes in the cleft dynamics, causing an expansion from 25 Å to 27 Å (Fig. S1 and Movie S2), alongside a slight reduction in the dihedral angle to -18°. To assess, which parts of the actin were most affected, we performed Root Mean Square Fluctuations analysis (RMSF) (see Methods) (Fig. 1C). We observed that the D-loop and SD4 subdomain showed distinctive differences in their RMSF profile. More precisely, the dynamics of helices encompassing residues 200-206 (H1 helix) and 228-232 (H2 helix), positioned at opposite sides of SD4, exhibited pronounced sensitivity to histidine methylation (Fig. 1D). Thus, taken together, this suggests that histidine 73 methylation impacts not only the local dynamics around the histidine residue but also regions distal from this site. Interestingly, although the sequence identity between α- and β-actin is very high (ca 94%), histidine methylation seemed to affect differently the amplitude of the dihedral-cleft fluctuations for α or β isoform (Fig. S2). The most affected areas in the α-actin were comparable to the ones seen in β-actin (Fig. S3). Furthermore, both the dihedral angle and the size of the cleft were exhibited a wider range of values in comparison to the β-actin isoform. This implies that β-actin undergoes more subtle changes compared to the α-actin isoform. These results highlight that slight modifications in the amino acid sequence between actin isoforms can be translated into detectable structural variations which may have impact on actin functions. For subsequent sections, we focus on the β-actin isoform, as limited information exists on the dynamics of this protein, despite of its importance (as introduced above).

Histidine 73 methylation opens the SD2-SD4 cleft and affects the enzymatic site. Next, we focused our analysis on dissecting specific structural perturbations in ATP-bound monomeric

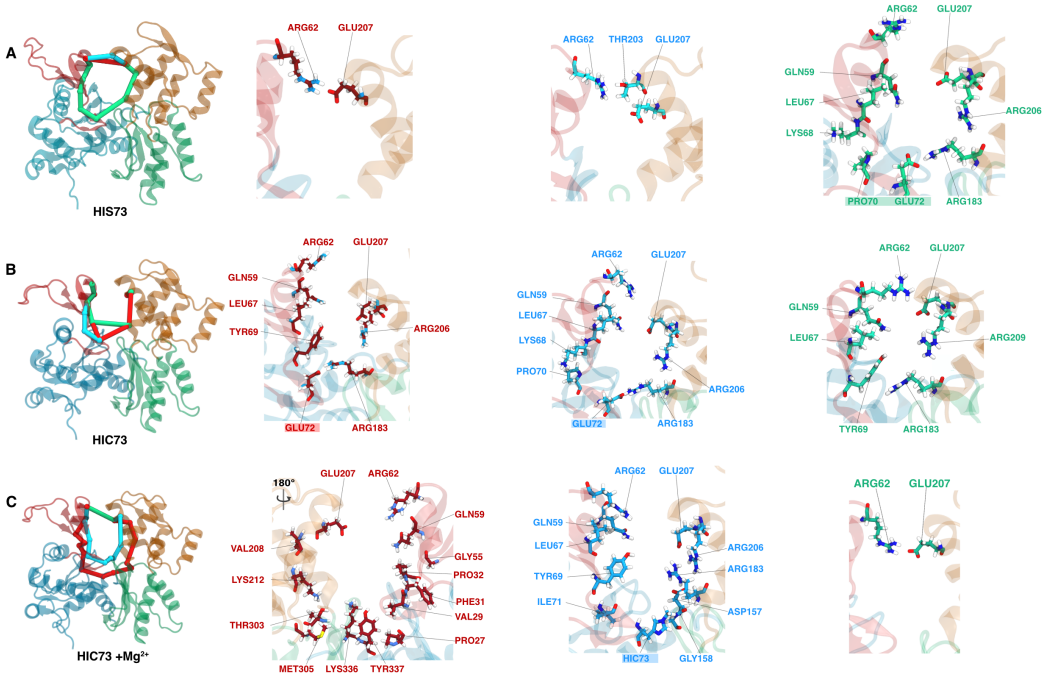

Figure 3. Main allosteric paths in ATP-bound β-actin systems. Representation of the three most represented between R62 and E207 for **A-** HIS73, **B-** HIC73 and **C-** HIC73+Mg^{2+} systems. Most represented path in red, second most represented in blue, and third most represented in green. On right, licorice representations of these three main paths using the same color scheme. Residues on the sensor loop are highlighted.

β-actin caused by histidine 73 methylation. We observed that in the case of unmethylated HIS73, residues of SD4 H1 helix interacted with residues from the SD2 domain, effectively bridging the two subdomains (Fig. 2A, left panel). Notably, GLU207 of SD4 formed stable interactions with residue ARG62 of SD2. Given the charged nature of these residues, these interactions are likely mediated via electrostatics. Additionally, based on the bond lengths and angles we measured, hydrogen bonding may also play a role. Regardless of the exact nature of this interaction, when we examined the same interactions in monomeric β-actin where HIS73 was methylated (HIC73), we noted that the likelihood of interaction between these amino acids was reduced (Fig. 2A, central panel), facilitating the opening of the cleft. This cleft opening was correlated with an increase of the active site volume (Fig. 2B-C) from 685 Å3 to 760 Å3. As this volume change may affect molecules inside the active site, we scrutinized the dynamic properties of the magnesium ion and water molecules around it. We observed two magnesium ion populations (Fig. 2D): a Mg^{2+} bound to the γ-phosphate, with a distance 2.2 Å between these two atoms, and an unbound Mg^{2+} at a distance of 4 Å from the γ-phosphate. For HIC73, the population of the Mg^{2+} in the bound state decreased. Surprisingly, we did not observed significant changes in the number of water molecules in the active site (Fig. 2E). Consequently, our results showed how the HIS73 methylation can affect subdomain interactions and active site for ATP-bound β-actin.

Histidine 73 methylation exerts allosteric effects to bridge SD2 and SD4 subdomains. Histidine 73 is situated at the core of the actin at the interface of all four subdomains (Fig. 1A). However, the mechanism through which the methylation of the residue influences distant regions, such as helices H1 and H2 on SD4, remains elusive. To elucidate this, we conducted correlation-based dynamical network analysis ***Westerlund et al.*** (***2020***); ***Melo et al.*** (***2020***). This analysis allows calculations of dynamic networks where nodes represent the alpha-carbons of each residue and the edges represent correlations of motions between nodes, and has been used to identify possible,

functionally relevant allosteric pathways ***Melo et al.*** (***2020***). Using this approach we identified several possible allosteric pathways between GLU207 and ARG62, the two residues engaged in the hydrogen bond that bridges SD2 and SD4 subdomains (Fig. 2A, left panels). In unmethylated monomeric β-actin (HIS73), two most represented allosteric paths involved direct interactions between GLU207 and ARG62 (Fig. 3A, left and central panels; Table S2), while the third path involved additional residues located on both SD2 and SD4 (Fig. 3A, right panel). Interestingly, the sensor loop was directly involved in this path through PRO70 and GLU72. Upon histidine methylation (HIC73 case), the direct interaction between GLU207 and ARG62 was lost, and replaced by interactions among a larger number of residues on SD2 and SD4 subdomains (Fig. 3B and Table S2). Notably, the sensor loop was involved in the two most representative paths, while the third one displayed an SD2-SD4 bridge mediated through interactions between TYR69 and ARG183 (Fig. 3B, right panel). Thus, change from HIS to HIC introduces measurable changes in allosteric network. We also observed that the ARG183 residue was involved in the most represented allosteric path in both HIS73 β-actin and HIC73 β-actin. To examine further whether a change in a single residue can introduce changes in allosteric networks, we performed simulations of the ARG183GLY mutant for HIC73 β-actin. We noted that in the ARG183GLY β-actin mutant the paths connecting SD2 and SD4 were redirected around the active site (Fig. S7B-D), which is distinct from what we saw in HIC73 β-actin, where they pass through the sensor loop. This rerouting was accompanied by a change of the cleft-dihedral profile (Fig. S7A). Taken together, these findings suggest that histidine 73 methylation promotes the opening of the cleft between SD2 and SD4 subdomains, which is otherwise held in a more closed conformation by the GLU207-ARG62 interaction. Histidine methylation, which changes the local polar environment, also alters allosteric paths that mediated interactions between SD2 and SD4, by rerouting allosteric communications away from direct hydrogen bonding between GLU207 and ARG62 and towards a more significant involvement of the sensor loop.

Presence of magnesium ions modulates the impact of histidine 73 methylation Magnesium ion concentration plays an important role in actin polymerization ***Kang et al.*** (***2012***). To examine whether histidine methylation is affected by magnesium ions we have performed simulations on the monomeric HIC73 β-actin using 75 mM of MgCl2 (to directly compare with 150 mM KCl). At this high Mg^{2+} ion concentration, both cleft and dihedral angles were affected, displaying an increase (up to 30 Å in cleft opening, and up to -30° dihedral angle, respectively) (Fig. 1B, right panel) in comparison to HIC73 system without magnesium ions. The RMSF (Fig. 1C) as well as the volume of the ATP binding site were affected by the addition of magnesium ions. The latter displayed a larger volume (Fig. 2C), although the distribution of water molecules in the active site remained unaffected (Fig. 2E). Additionally, the population of magnesium ion not bound to the γ-phosphate slightly increased (Fig. 2D). We also used a larger simulation box of c.a. 100,000 atoms (see Table S1) to simulate a system with a molar concentration of 7.5 mM MgCl2 (corresponding to 5 Mg^{2+} ions), which is similar to the concentration used for *in vitro* actin polymerization assays ***Kang et al.*** (***2012***). At this Mg^{2+} ion concentration, we also observed increases in both cleft and dihedral angles (Fig. S4), albeit less pronounced than the one seen for 75 mM of MgCl2. Attempting a concentration of 75 mM of MgCl2 for this larger system size, we observed even larger modulations of the cleft-dihedral profile (Fig. S4). Thus, monomeric actin flexibility is dependent of the magnesium ion concentration. Magnesium (as well as potassium) ions were interacting on numerous sites spread on different subdomains (ASP56, GLU93, GLU99, GLU100, GLU270, and GLU364; Fig. S5). Lastly, we examined how magnesium ions affect the allosteric paths between SD2 and SD4 in methylated G-actin (Fig. 3C). Interestingly, the most represented path was no longer passing through the sensor loop, but on the opposite side of the active site. Hence, the addition of magnesium ions modulates the effects of H73 methylation and rebalances allosteric pathways in a way that mirrors what we observed in unmethylated G-actin.

ADP binding reduces the impact of histidine 73 methylation on actin dynamics To investigate whether the effects of HIS73 methylation are dependent on the nature of the bound

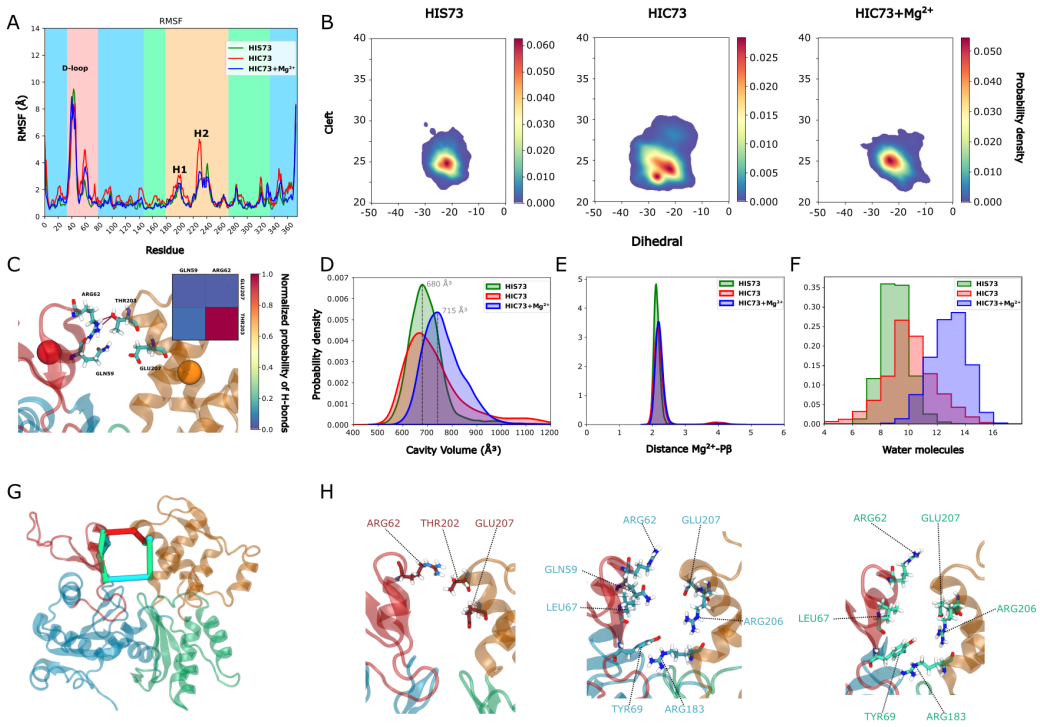

Figure 4. ADP reduces the β-actin dynamics. A- RMSF of ADP-Actin systems. Background colors correspond to subdomains (see Figure 1). **B-** Cleft-Dihedral maps of ADP bound actin systems. **C-** Main hydrogen bonds between SD2 and SD4 subdomains for HIC73 system. **D-** Volumes of active sites. **E-** Distribution of the distance between magnesium ion and γ-phosphate. **F-** Histograms of the number of water molecules around the magnesium ($\leq$ 5 Å) in the active site. **G-** Representation of three most represented allosteric paths between R62 and E207 in HIC73 system. **H-** Licorice representation of the residues involved in the three main paths presented in G. Pathways for HIS73 and HIC73+Mg^{2+} systems are presented in Figure S4. Differences observed between HIS73, HIC73, and HIC+Mg^{2+} systems are all significant except for the the distance between magnesium ion and γ-phosphate (Table S3).

nucleotide, we performed additional simulations with ADP in the binding cavity, providing a basis for comparison with ATP-bound actin. In the presence of ADP, the internal flexibility of the actin monomer, particularly in the SD4 subdomain, was reduced for methylated H73, as revealed by the RMSF profile (Fig. 4A), although the dynamics of the H2 helix (residues 228-232) still remained enhanced. Additionally, when compared to ATP-bound state, ADP-binding led to decrease in the cleft opening in HIC73, and HIC73 with addition of Mg^{2+} (Fig. 4B). This difference can be explained by sustained interactions between residues at the SD2-SD4 interface (Fig. 4C and Fig. S6). We observed that when ADP is bound, the volume of the active site exhibited reduced fluctuations (Fig. 4D). In all our conditions (HIS73, HIC73, HIC73+Mg^{2+}), the magnesium ion in the binding site was directly bound to the nucleotide (Fig. 4E), despite variations in the number of water molecules around the ion (Fig. 4F). Finally, the binding of ADP also affected the allosteric paths between SD2 and SD4 by involving a direct interaction between ARG62 and GLU207 (Fig 4. G,H and Fig. S6), or by passing through TYR69-ARG183. Thus, in the conditions observed in our simulations, the binding of ADP reduced the impact of histidine 73 methylation on actin plasticity.

Impact of the deafness-causing mutation on histidine 73 methylated actin dynamics. The mutation of lysine 118 into asparagine (LYS118ASN) has been shown to cause deafness ***Rubenstein and Wen*** (***2014***), most likely due to its impact on the rate of actin polymerization and nucleation ***Ali et al.*** (***2022***); ***Kruth and Rubenstein*** (***2012***). However, whether histidine 73 methylation status influences the extent to which this mutation affects actin behavior has not been examined. To

have a better comprehensive view on the influence of this mutation on actin filament nucleation, we conducted simulations with LYS118ASN actin in the presence of both ATP or ADP and HIS73 methylation (HIC73). In the presence of ATP, the cleft-dihedral profile (Fig. S2) revealed a more open state, yet more focused, closely resembling conformations seen in the case of HIC73 with addition of magnesium ions. Interestingly, for bound ATP, the actin flexibility was also reduced (Fig. S3) compared to the wild type HIC73. This suggests that the LYS118ASN mutation not only induces a more open conformation but also imparts a degree of structural rigidity to the actin filament in the presence of ATP. Conversely, in the presence of ADP, the mutation had a very low impact on the cleft-dihedral map.

Histidine 73 methylation stabilizes F-actin at the barbed end Transition from G-actin to F-actin that accompanies actin polymerization is essential for cellular function. To understand the impact of H73 methylation on F-actin assembly and dynamics, as a function of nucleotide binding, we analyzed conformational dynamics of actin subunits at the barbed end of the filament. Simulations were performed on the four F-actin subunits, with the two subunits towards the pointed end constrained to mimic a longer filament, and two on the barbed (growing) end free to sample broad conformational space (see details in the Method section). For all the subunits, H73 was either methylated (HIC73) or non-methylated (HIS73), and the active site contained either ATP or ADP. Utilizing 1.52 μs of polarizable MD simulations with adaptive sampling, we explored the dynamics of the last (B) and penultimate (B-1) subunits at the barbed end (Fig. 5A), which have been reported to experience major deformations ***Zsolnay et al.*** (***2020***). In the methylated system, the last F-actin (B) subunit exhibited more pronounced deformation when ADP was bound, than in the presence of ATP (Fig. S9A), which is in contrast to what we observed in G-actin. Specifically, with ADP bound, the cleft-dihedral profile of HIC73 displayed conformations resembling those observed for HIS73 G-actin monomers (Fig. 4B). The penultimate (B-1) subunit appeared less affected by the nucleotide state, probably due to a higher number of contacts with the other subunits in the filament (Fig. S8 and Fig. S9B). For both B and B-1 subunits, the dynamics of the H1 helix was the most affected in comparison to the monomeric form (Fig. S9). For HIC73, in the B subunit, this helix strongly interacted with the C-terminal residues of the B-1 subunit for bound ADP but not in the case of ATP (Fig. S10). Both ATP- and ADP-bound HIS73 systems were less stabilized in the F-actin conformation than the ATP-bound HIC73 system (Fig. 5B). We also observed more interactions between the C-terminal part of the B-1 subunit and the H1 helix of the B subunit in these systems (Fig. S10). These results showed that H73 methylation also modulated multiple different aspects of F-actin plasticity, further highlighting the biological significance of this PTM.

Histidine 73 methylation reduces the opening of a molecular backdoor at the barbed end. Molecular dynamics simulations were recently used to propose two plausible pathways for the release of inorganic phosphate (Pi) after ATP hydrolysis in the F-actin state ***Oosterheert et al.*** (***2023***). The first pathway involves the breaking of the interaction between ARG177 and ASN111, and was experimentally validated, while the second one requires breaking of the SER14-GLY74 interaction (see Fig. 5C) ***Chou and Pollard*** (***2019***). This pathway remains to be experimentally demonstrated. Based on our simulations, this second backdoor was mainly closed in the presence of methylated histidine, and open for non-methylated histidine in the ATP-bound state of both B (Fig. 5D) and B-1 (Fig. 5E) actin subunits. Interestingly, the reanalysis of the data openly deposited by the Hummer lab ***Oosterheert et al.*** (***2023***) (see Method section) agreed well in term of opening and closing distances for this second backdoor (Fig. 5D,E). This model additionally proposed that the ARG177-ASN111 interaction was always open for the last actin subunit ***Oosterheert et al.*** (***2023***). We also observed that this backdoor remains open in the last subunit, independently of the histidine methylation (Fig. S11). To test the impact of the histidine methylation on the release of Pi within F-actin subunits, we performed *in vitro* actin filament depolymerization assays using microfluidics ***Jégou et al.*** (***2011***) (Fig 5-F, see Methods). We observed that the Pi release rate was almost 3-fold lower for

histidine-methylated β-actin compared to the non-methylated one (Fig. 5G and Fig. S12). Our data, together with the recent observations ***Oosterheert et al.*** (***2023***), indicate that histidine methylation controls the release of Pi in F-actin, mainly by delaying the opening of the SER14-GLY74 backdoor.

Discussion

In this study, we performed a series of adaptive sampling simulations using a polarizable force field on 17 different actin systems (Table S1), reaching a total time of simulation of more than 25 µs. Although actin has been extensively studied using classical computational strategies ***Splettstoesser et al.*** (***2009***); ***Saunders and Voth*** (***2011***); ***Saunders et al.*** (***2014***); ***McCullagh et al.*** (***2014***); ***Jepsen and Sept*** (***2020***); ***Chu and Voth*** (***2005***); ***Hocky et al.*** (***2016***); ***Jepsen and Sept*** (***2020***); ***Zsolnay et al.*** (***2020***) this work represents the first study of actin using polarizable forcefields, which improves accuracy of modeling interatomic interactions. This accuracy, in turn, enables more accurate insights into molecular determinants of conformational changes and dynamics that accompany actin assembly and function. Notably, the barbed end models, containing more than 250k atoms, represent, to the best of our knowledge, one of the largest systems being modelled with this type of forcefield and for such extended timescale.

Although focusing our core interest on β-actin, as a more prevalent yet less understood actin isoform, we used α-actin to benchmark our approach. Overall, our results for this isoform are in broad agreement with previous atomistic simulations ***Jepsen and Sept*** (***2020***); ***Saunders et al.*** (***2014***), supporting the validity of polarizable forcefield approach. For example, in our study the cleft distance varied from 23 to 25 Å in the ATP state, which is similar to what was seen by Saunders et al. ***Saunders et al.*** (***2014***). However, we note that the dihedral angle values varied among the studies: -18 to -23 degrees for Saunders *et al.* ***Saunders et al.*** (***2014***), -11.7 degrees in recent work by Jepsen et al. ***Jepsen and Sept*** (***2020***), and -12 to -18 degrees in our calculations. Some of this variability may be due to the intrinsic difference between the results obtained using of a polarizable force field and those from non-polarizable atomistic force field simulations, as recently demonstrated for other proteins ***El Ahdab et al.*** (***2021***). Importantly, our simulations revealed that α- and β-actin exhibited distinct patterns of flexibility, suggesting that these differences may explain functional differences that exist despite exceptionally high level of sequence identity. Differences observed in our simulations are consistent with a significant difference in phosphate release rate between α-actin and β-actin, the latter releasing its phosphate slightly faster ***Jégou et al.*** (***2011***) (Fig S12). Therefore, our study hints at protein dynamics as the key difference between otherwise almost identical actin isoforms expressed by mammals.

In addition to expanding our understanding of β-actin, we also addressed the role of a highly conserved, yet relatively incompletely understood PTM, H73 methylation ***Kwiatkowski et al.*** (***2018***); ***Wilkinson et al.*** (***2019***). Recent studies have shown that unmethylated actin shows an increased rate of nucleotide exchange in the monomeric form, and a slower filament assembly rate ***Wilkinson et al.*** (***2019***); ***Guo et al.*** (***2019***). Additionally, H73 methylation was shown to increase actin filament stability ***Kwiatkowski et al.*** (***2018***). Our results showed an enhanced internal dynamics of the methylated actin monomer in the ATP state which may account for these previous observations. Our simulations of the β-actin isoform highlighted a wider opening of the cleft between SD2 and SD4 subdomains in the G-actin form due to the disruption of direct interactions between ARG62 and GLU207. This opening may have implications during the early steps required for the nucleation of actin filaments. As ARG62 and GLU207 residues are also involved in inter-subunits interactions in the filament, they thus need to be rearranged accordingly ***Oda et al.*** (***2009***). Based on our results, we speculate that direct interactions between ARG62 and GLU207 may affect interactions between actin subunits, thereby limiting the nucleation process.

We also examined mutual relationships between H73 methylation and environmental factors, such as magnesium ions and nucleotides. In general, we observed that actin plasticity is affected not only by H73 methylation, but by other factors as well. Most notably, ADP binding may lock the actin monomer in an closed state, impeding G-actin structural adaptation at the filament barbed

end. It is therefore reasonable to think that interactions between intra-monomer residues may compete with interactions between inter-monomer residues both during the nucleation and elongation of filaments. Our results demonstrate how histidine methylation affects these essential interactions. Finally, histidine methylation may also play a role in stabilizing subunits at the barbed end, as in the absence of methylation, the last subunit tends to relax more quickly towards the G-actin form

Using correlation-based dynamical network analysis we were able to link actin flexibility with distinct allosteric paths between the SD2 and SD4 subdomains of β-actin, which are critical for defining the size and openness of the nucleotide binding cleft, and thus ATP hydrolysis. This led to the insight that in the case of ATP-bound methylated G-actin, the main allosteric paths were re-routed through the sensor loop. Conversely, allosteric paths observed in the ADP-bound states almost never involved this loop, minimizing the impact of histidine methylation on SD2-SD4 mobility. Altogether, these results offer initial insights into how allosteric paths drive local molecular rearrangements in the active site towards large conformational changes at the actin filament ends, and how they may fine-tune mechanical properties of actin filaments ***De La Cruz et al.*** (***2010***); ***Reynolds et al.*** (***2022***). This may further inform our understanding of why side-binding proteins, such as ADF/cofilin, are highly sensitive to both the nucleotide state of actin filaments and their mechanical state ***Cao et al.*** (***2006***); ***Wioland et al.*** (***2017***, 2019); ***Lappalainen et al.*** (***2022***).

Our results also highlighted that H73 methylation increases the volume of the active site, without changing the number of water molecules inside the active site. This may indicate that methylation influences the structuring of the water network that participates in ATP hydrolysis ***McCullagh et al.*** (***2014***); ***Kanematsu et al.*** (***2022***), rather than the amount of water molecules available. Our results also highlight that histidine methylation tunes Pi release. The Pi release rate within filaments is faster for non-methylated β-actin, which may be related to the opening of more than one backdoors, as further revealed by our simulations at the filament barbed end.

Overall, our results highlighted how the post translational modification of histidine 73 can drastically change the dynamic properties of actin in different forms, from the monomer to the filament. Furthermore, effects of H73 methylation and environmental factors seem to be tightly coupled, and exert mutual, functionally relevant modulations. Thus, our work reveals how subtle structural changes, such as a simple methylation buried within the core of the protein, could have numerous consequences that affect protein plasticity at different scales. Importantly, although understudied, histidine methylation has now been reported in other proteins, such as S100A9, myosin, skeletal muscle myosin light chain kinase (MLCK 2), and ribosomal protein Rpl3 ***Kwiatkowski and Drozak*** (***2020***), with a recent analysis identifying about 300 histidine methylation sites in the proteome of HeLa cells ***Kapell and Jakobsson*** (***2021***). Similar to what we observed in β-actin, we expect that this PTM plays a major regulatory role in many of these systems. Thus, our study highlights the value of using MD simulations combined with polarizable forcefields as a method for understanding the effects of this PTM in actin and beyond.

Methods and Materials

Systems preparation

The initial structures of the Actin monomer in the ATP and ADP were obtained from the 1NWK ***Graceffa and Dominguez*** (***2003***) and 1J6Z ***Otterbein et al.*** (***2001***) pdb structures respectively. In the ATP state, the α and β-actin sequences were used. As the N-terminal acetylation or arginylation of the β-actin is known to have diverse biological effects ***Varland et al.*** (***2019***); ***Chen and Kashina*** (***2021***), we decided to remove the N-terminal amino acid, starting our β-actin sequence at ASP2.

The N-terminal and C-terminal extremities and the D-loop were generated using modeller ***Šali and Blundell*** (***1993***). In the original pdb files, the nucleotide is under the form of AMP and in presence of a calcium ion. We replaced the AMP by ATP and the calcium ion by a magnesium ion, to be closer to physiological conditions.

It has been demonstrated that crystallographic water molecules located inside the cavity may impact the behaviour of the protein ***Saunders and Voth*** (***2011***). Therefore, the water molecules placed at less than 10Åof the magnesium ion were kept.

In addition to the monomer systems, two 4-mer systems were prepared based on the 6BNO ***Gurel et al.*** (***2017***) pdb file, in presence of ADP and ATP. For the ATP state, the ADP has been replaced by ATP. The N-terminal and C-terminal extremities only were generated using modeller.

For all systems, the residues have been protonated following the results of PROPKA3 ***Olsson et al.*** (***2011***). All systems were solvated in water boxes using the xyzedit tool of the Tinker-hp distribution ***Rackers et al.*** (***2018***), so that there was at least 20Åbetween two images of the protein. The systems were then neutralized and KCL atoms were added to reach 150mM concentration. Regarding the simulations at high Mg^{2+} ions concentrations, all K+ atoms were replaced by half number of Mg^{2+} ions.

The force field parameters used for the protein parameters was the AMOEBA Polarizable force field for proteins ***Shi et al.*** (***2013***). Previously published parameters were used for the ATP and ADP systems ***Walker et al.*** (***2020***). The parameters of the HIC73 residues were developed following the procedure used to develop the AMOEBA force field for proteins. All QM calculations were performed using Gaussian09 ***Frisch et al.*** (***2009***). The model residue used to develop the parameters was a dipeptide Ac-HIC-NME were the Ac, NME and backbone parameters were extracted from the AMOEBABIO18 force field ***Zhang et al.*** (***2018***). Briefly, geometry optimisation were carried out at the MP2/6-31G* level. Initial atomic multipoles were derived at the MP2/6-311G** level using the Distributed Dipole Analysis (DMA) procedure ***Stone*** (***1981***). The resulting atomic multipôles were optimized against MP2/aug-cc-pvtz electrostatic potential on a set of grid points distributed around the dipeptide. During this fitting, the monopoles were held fixed. The point charges were adjusted at the junction atom between the backbone and the sidechain (adjustment of 0.03 on the -CH2- carbon atom charge), to insure electrical neutrality. As realised in the original AMOEBA for protein publication, 3 conformations were used to realize the fitting of the dipôle and multipôle components. The valence,vdW and torsional parameters were extracted from the AMOEBA parameters of the classical HIS residue.

Simulation setup

All molecular dynamics simulations were performed using the GPU version of the Tinker-HP software ***Adjoua et al.*** (***2021***). During the calculations, periodic boundary conditions were employed using the Particle Mesh Ewald method. The van der Waals and PME cutoffs were respectively of 12Åand 7Å. An analytical long range correction of the vdW interactions has been used. The dipole convergence criterion of the preconditioned conjugate gradient polarization solver was set to 0.01 Debye/atom for the minimization steps, and to 0.00001 Debye/atom otherwise.

For the minimization steps, no polarization or electrostatics terms were used. The systems underwent a minimization of 30 000 step using a L-BFGS optimizer. The next equilibration steps were realised using a timestep of 1fs, the RESPA integrator and the berendsen barostat (when relevant) unless stated otherwise. The solvent was then progressively heat up in the NVT ensemble, from 5K to 300K using 10K steps and spending 5ps at each temperature, before undergoing additional 100ps at 300K. The system was then allowed to slowly relax for 3 times 400ps in the NPT ensemble while applying harmonic restraints of 10, 5 and finally 1 kcal/mol/A on the backbone atoms of the protein. Then, all restraints were removed, and we used the montecarlo barostat in combination with the BAOAB-RESPA1 ***Lagardère et al.*** (***2019***) propagator. Three final equilibration steps were performed for 100ps, 200ps and 500 ps by respectively increasing the outer timestep from 1fs to 2fs up to 5fs.

Regarding the production run, all calculations were performed in the NPT ensemble, using the montecarlo barostat and the BAOAB-RESPA1 propagator with an outer timestep of 5fs, and hydrogen mass repartioning. A first 10ns simulations was performed to generate a first set of structures. In order to maximize the phase space exploration, we then resorted to an adaptive sampling pro-

Table 1. Number of seeds of each round of Adaptive sampling.

1st	2nd to 10th	total simulation time
8*10ns	16*10ns	1.52µs

cedure: a certain number of structures were first extracted from this initial simulation to perform the first adaptive sampling round. The seeds were then chosen following a procedure already described in ***Jaffrelot Inizan et al.*** (***2021***). Briefly, a principal component analysis is performed on the 10ns simulation using the scikit-learn ***Pedregosa et al.*** (***2011***) and MDTraj ***McGibbon et al.*** (***2015***) packages from which the n=4 first principal modes are considered (note:10 modes are calculated). The density ρ_k of the conformational space is then projected on the 4 modes and approximated using a Gaussian density kernel estimator:

$$\rho_k(x_i) = \frac{1}{(2\pi\sigma^2)^{n/2} M_k} \sum_{i=1}^{M_k} \exp - \frac{|x - x_i|^2}{2\sigma^2} \tag{1}$$

With the σ bandwith being chosen with the D.W Scott method of Scipy***Virtanen et al.*** (***2020***), M_k being the total number of configurations, x_i the orthogonal projection of the configuration on the n PCA modes. Then a bias is introduced to the selection of a new seed x_i under the following form :

$$P(i) = \frac{\rho_k^{-1}(x_i)}{\sum_{j=1}^{M_k} \rho_k^{-1}(x_j)} \tag{2}$$

The probability of selecting the x_i structure is inversely proportional to its density, projected on the first 4 PCA components, favoring new, undiscovered structural states.

Following this, 10 ns simulations were run to form the new phase space of structures for the next adaptive sampling round. For each following round, all simulations are added to the conformational space on which the next adaptive sampling are performed. The number of seeds used for each round is summed up in Table 1.

Regarding the 4-mer systems, we were interested in the behaviour of the barbed end only. For this extremity, it has recently been demonstrated that the behaviour of the B and B-1 residues is different than other residues of the filament ***Zsolnay et al.*** (***2020***). Therefore, to simulate the behaviour of this extremity only, the backbone atoms of two monomers forming the pointed end have been constrained using a 10kcal/mol restraint. This way, it was possible to study the evolution of the barbed end in a constrained filament, while keeping the sidechains free. 1.52 µs long simulations were generated on thirteen monomer systems and four 4-mer systems, resulting in a total of 25.84 µs (see Table S1).

Molecular Dynamics Analysis

For analysis, the data were collected each 100 ps of simulation. Measures have been performed using the VMD software***Humphrey et al.*** (***1996***).

The Root Mean Square Fluctuations of an amino acid i has been defined as previously described ***Welford*** (***1962***):

$$RMSF_i = \sqrt{< (x_i - x_{moy})^2 >} \tag{3}$$

with x_i the position of the center of mass of the backbone of the amino acid *i* at a certain frame, and x_{ref} its ensemble averaged position.

Active site volumes have been computed using E-pock program ***Laurent et al.*** (***2015***). We first defined a Maximum Encompassing Region (MER) by concatenating spheres to define the maximum volume of the active site as followed: a 6Å sphere around the N1, N9, PA, PG (PB for ADP) atoms

Table 2. Definition of each subdomain

	SD1	SD2	SD3	SD4
Residues	5-33 80-147 334-349	34-39 52-69	148-179 273-333	180-219 252-262

of the nucleotide and one additional sphere around the Mg^{2+} ion coordinated to it. Then, for each frame of the trajectory, E-pock calculated a 3D grid based on the MER and removed grid cells which were overlapping with residues from the active site. The remaining cells defined the free volume of the active site.

Shortest paths have been calculated using the Dynamical Network Analysis (Dynetan) tool ***Melo et al.*** (***2020***). This program allowed defining nodes based on residues alpha carbons. The minimum distance between two nodes was measured on each frame of the simulation. If this distance is lower than 4.5 Å for more than 75% of the simulation, the two nodes were considered in contact. Once all nodes in contact were determined, correlation of motion was calculated between them to create the optimal correlation paths. For the calculation of allosteric paths, the shortest path of each seed has been calculated on the 10ns. Then all found shortest paths were reweighted across all seeds, and the 3 highest shortest paths have been kept for figures. All shortest paths accounting for more than 3 percent of all paths are available in supplementary information.

The dihedral and cleft angle has been defined following the work of Saunders and coworkers ***Saunders et al.*** (***2014***): Dihedral = SD2-SD1-SD3-SD4, Cleft = SD2-SD4 distance. To caculate these values, the center of mass of each subdomains have been defined as displayed in table2.

Each of the observable had to be reweighted to take into account the bias introduced by the adaptive sampling. For this purpose, the unbiasing factor α_i of each seed is defined as :

$$\alpha_i = \frac{1}{M_k P(i)} \tag{4}$$

The final weight of each seed is then :

$$\omega_i = \frac{\alpha_i}{\sum_j \alpha_j} \tag{5}$$

We reanalysed data from the Hummer lab available at: https://zenodo.org/records/7765025 ***Blanc*** (***2023***). We have used the trajectory called replica_031 from the dataset: simulations_dataset_1/Metady-namics/BarbedEnd_meH73p/representative_trajectories corresponding to the Hummer lab enhanced sampling protocol based on simulating *swarms* of short metadynamics trajectories to open the second physically plausible pathways ***Okazaki and Hummer*** (***2013***). By methodological means, the G74-S14 backdoor was closed in the initial half of the simulation (metaD_i) and then open in the final half of the simulation (metaD_f).

In vitro measurement of Pi-release rate

Human cytoplasmic β-actin was expressed and purified from yeast *Pichia Pastoris*, following established protocol ***Hatano et al.*** (***2020***). Actin was cotransfected with the N-acetyl transferase NAA80, and with or without histidine methyltransferase SETD3, for N-terminal acetylation and His73 methylation respectively.

In vitro fluorescence microscopy experiments were performed in microfluidic chambers, as described in ***AU Wioland et al.*** (***2022***). Briefly, tens of single actin filaments were polymerized for 10-15 min from surface-anchored spectrin-actin seeds with a solution containing 1 µM monomeric β-actin, 1 µM human profilin and 0.5-1 µM ATP-ATTO ***Colombo et al.*** (***2021***) in F-buffer (10 mM Tris HCl pH 7.4, 50 mM KCl, 1 mM MgCL2, 0.2 mM EGTA, 0.2 mM ATP, 10 mM DTT, 1 mM DABCO) supplemented with 50 mM KPO4 buffer pH 7.4 to maintain actin in an ADP-Pi state. Filaments were

then exposed from time t=0 to F-buffer only (without KPO4), triggering their barbed-end depolymerization and Pi release from actin subunits. Images were acquired on a Nikon Ti microscope, 60x objective, X-cite Exact lamp and Orca Flash 4.0 camera, at 1 frame every 2 to 5 s.

Movies were analyzed with a custom-made Python algorithm (available upon request) which tracks the depolymerizing barbed end of each filament (used packages: numpy, scipy, matplotlib, trackpy). For each filament, the spontaneous depolymerization rate was measured from the linear fit of the barbed-end position over 5 frames. The data of at least 30 filaments were pooled and the depolymerization rate over time was fitted (scipy function "curve-fit") as ***Jégou et al.*** (***2011***):

$$v_{depol}(t) = \left[e^{-k_{off} \times t} \left(\frac{1}{v_{depol}^{ADP-Pi}} - \frac{1}{v_{depol}^{ADP}} \right) + \frac{1}{v_{d}^{ADP} epol} \right]^{-1} \tag{6}$$

with free parameters k_{off} the Pi release-rate, v_{depol}^{ADP-Pi} and v_{depol}^{ADP} the barbed-end depolymerization rates of ADP-Pi- and ADP-actin, respectively.

Data Availability

Data deposition: MD simulation material and scripts for visualisation are available at https://doi.org-/10.5281/zenodo.10055504

Acknowledgments

A. D. is funded by the ITMO Cancer of Aviesan "Mathematiques et Informatique". This work has also received funding from the European Research Council (ERC) under the European Union's Horizon 2020 research and innovation program (grant agreement No 810367), project EMC2 (JPP). This work was granted access to the HPC resources of CALMIP supercomputing center (under the allocation 2021-P21020) and TGCC Joliot-Curie supercomputer (under the GENCI allocation A0110712941).

References

Adjoua O, Lagardère L, Jolly LH, Durocher A, Very T, Dupays I, Wang Z, Inizan TJ, Célerse F, Ren P, Ponder JW, Piquemal JP. Tinker-HP: Accelerating Molecular Dynamics Simulations of Large Complex Systems with Advanced Point Dipole Polarizable Force Fields Using GPUs and Multi-GPU Systems. Journal of Chemical Theory and Computation. 2021; 17(4):2034–2053. doi: 10.1021/acs.jctc.0c01164.

Ali R, Zahm JA, Rosen MK. Bound nucleotide can control the dynamic architecture of monomeric actin. Nature Structural & Molecular Biology. 2022 Apr; 29(4):320–328. https://doi.org/10.1038/s41594-022-00743-5, doi: 10.1038/s41594-022-00743-5.

AU Wioland H, AU Ghasemi F, AU Chikireddy J, AU Romet-Lemonne G, AU Jégou A. Using Microfluidics and Fluorescence Microscopy to Study the Assembly Dynamics of Single Actin Filaments and Bundles. JoVE. 2022 May; 183(183):e63891. https://www.jove.com/t/63891, doi: 10.3791/63891.

Bellissent-Funel MC, Hassanali A, Havenith M, Henchman R, Pohl P, Sterpone F, van der Spoel D, Xu Y, Garcia AE. Water Determines the Structure and Dynamics of Proteins. Chemical Reviews. 2016; 116(13):7673–7697. https://doi.org/10.1021/acs.chemrev.5b00664, doi: 10.1021/acs.chemrev.5b00664, pMID: 27186992.

Blanc FEC, MD Simulations Molecular mechanisms of inorganic-phosphate release from the core and barbed end of actin filaments, https://doi.org/10.5281/zenodo.7765025. Zenodo; 2023. https://doi.org/10.5281/zenodo.7765025, doi: 10.5281/zenodo.7765025.

Blanchoin L, Pollard TD. Hydrolysis of ATP by Polymerized Actin Depends on the Bound Divalent Cation but Not Profilin. Biochemistry. 2002 Jan; 41(2):597–602. https://doi.org/10.1021/bi011214b, doi: 10.1021/bi011214b.

Bowman GR, Ensign DL, Pande VS. Enhanced Modeling via Network Theory: Adaptive Sampling of Markov State Models. Journal of Chemical Theory and Computation. 2010; 6(3):787–794. https://doi.org/10.1021/ct900620b, doi: 10.1021/ct900620b, pMID: 23626502.

Bunnell TM, Burbach BJ, Shimizu Y, Ervasti JM. β-Actin specifically controls cell growth, migration, and the G-actin pool. Molecular Biology of the Cell. 2011; 22(21):4047–4058. https://doi.org/10.1091/mbc.e11-06-0582, doi: 10.1091/mbc.e11-06-0582, pMID: 21900491.

Cao W, Goodarzi JP, De La Cruz EM. Energetics and kinetics of cooperative cofilin-actin filament interactions. J Mol Biol. 2006 Aug; 361(2):257–267.

Castaneda N, Lee M, Rivera-Jacquez HJ, Marracino RR, Merlino TR, Kang H. Actin Filament Mechanics and Structure in Crowded Environments. The Journal of Physical Chemistry B. 2019; 123(13):2770–2779. https://doi.org/10.1021/acs.jpcb.8b12320, doi: 10.1021/acs.jpcb.8b12320, pMID: 30817154.

Ceron RH, Carman PJ, Rebowski G, Boczkowska M, Heuckeroth RO, Dominguez R. A solution to the long-standing problem of actin expression and purification. Proceedings of the National Academy of Sciences. 2022; 119(41):e2209150119. https://www.pnas.org/doi/abs/10.1073/pnas.2209150119, doi: 10.1073/pnas.2209150119.

Chen L, Kashina A. Post-translational Modifications of the Protein Termini. Frontiers in Cell and Developmental Biology. 2021; 9. https://www.frontiersin.org/articles/10.3389/fcell.2021.719590, doi: 10.3389/fcell.2021.719590.

Chou SZ, Pollard TD. Mechanism of actin polymerization revealed by cryo-EM structures of actin filaments with three different bound nucleotides. Proceedings of the National Academy of Sciences of the United States of America. 2019 03; 116(10):4265 – 4274. https://www.pnas.org/content/116/10/4265, doi: 10.1073/pnas.1807028115.

Chu JW, Voth GA. Allostery of actin filaments: Molecular dynamics simulations and coarse-grained analysis. Proceedings of the National Academy of Sciences. 2005; 102(37):13111–13116. https://www.pnas.org/doi/abs/10.1073/pnas.0503732102, doi: 10.1073/pnas.0503732102.

Colombo J, Antkowiak A, Kogan K, Kotila T, Elliott J, Guillotin A, Lappalainen P, Michelot A. A functional family of fluorescent nucleotide analogues to investigate actin dynamics and energetics. Nature Communications. 2021 Jan; 12(1):548. https://doi.org/10.1038/s41467-020-20827-4, doi: 10.1038/s41467-020-20827-4.

Célerse F, Inizan TJ, Lagardère L, Adjoua O, Monmarché P, Miao Y, Derat E, Piquemal JP. An Efficient Gaussian-Accelerated Molecular Dynamics (GaMD) Multilevel Enhanced Sampling Strategy: Application to Polarizable Force Fields Simulations of Large Biological Systems. Journal of Chemical Theory and Computation. 2022; 18(2):968–977. doi: 10.1021/acs.jctc.1c01024, pMID: 35080892.

Célerse F, Lagardère L, Derat E, Piquemal JP. Massively Parallel Implementation of Steered Molecular Dynamics in Tinker-HP: Comparisons of Polarizable and Non-Polarizable Simulations of Realistic Systems. Journal of Chemical Theory and Computation. 2019; 15(6):3694–3709. https://doi.org/10.1021/acs.jctc.9b00199, doi: 10.1021/acs.jctc.9b00199, pMID: 31059250.

De La Cruz EM, Roland J, McCullough BR, Blanchoin L, Martiel JL. Origin of twist-bend coupling in actin filaments. Biophys J. 2010 Sep; 99(6):1852–1860.

Dugina VB, Shagieva GS, Shakhov AS, Alieva IB. The Cytoplasmic Actins in the Regulation of Endothelial Cell Function. International Journal of Molecular Sciences. 2021; 22(15). https://www.mdpi.com/1422-0067/22/15/7836, doi: 10.3390/ijms22157836.

El Ahdab D, Lagardère L, Inizan TJ, Célerse F, Liu C, Adjoua O, Jolly LH, Gresh N, Hobaika Z, Ren P, Maroun RG, Piquemal JP. Interfacial Water Many-Body Effects Drive Structural Dynamics and Allosteric Interactions in SARS-CoV-2 Main Protease Dimerization Interface. The Journal of Physical Chemistry Letters. 2021; 12(26):6218–6226. doi: 10.1021/acs.jpclett.1c01460, pMID: 34196568.

El Khoury L, Jing Z, Cuzzolin A, Deplano A, Loco D, Sattarov B, Hédin F, Wendeborn S, Ho C, El Ahdab D, Jaffrelot Inizan T, Sturlese M, Sosic A, Volpiana M, Lugato A, Barone M, Gatto B, Macchia ML, Bellanda M, Battistutta R, et al. Computationally driven discovery of SARS-CoV-2 Mpro inhibitors: from design to experimental validation. Chem Sci. 2022; 13:3674–3687. http://dx.doi.org/10.1039/D1SC05892D, doi: 10.1039/D1SC05892D.

Frisch MJ, Trucks GW, Schlegel HB, Scuseria GE, Robb MA, Cheeseman JR, Scalmani G, Barone V, Mennucci B, Petersson GA, Nakatsuji H, Caricato M, Li X, Hratchian HP, Izmaylov AF, Bloino J, Zheng G, Sonnenberg JL, Hada M, Ehara M, et al., Gaussian 09 Revision A.2; 2009.

Graceffa P, Dominguez R. Crystal structure of monomeric actin in the ATP state: Structural basis of nucleotide-dependent actin dynamics. Journal of Biological Chemistry. 2003; 278(36):34172–34180. http://dx.doi.org/10.1074/jbc.M303689200, doi: 10.1074/jbc.M303689200.

Guo C, Liu S, Wang J, Sun MZ, Greenaway FT. ACTB in cancer. Clinica Chimica Acta. 2013; 417:39–44. https://www.sciencedirect.com/science/article/pii/S0009898112005839, doi: https://doi.org/10.1016/j.cca.2012.12.012.

Guo Q, Liao S, Kwiatkowski S, Tomaka W, Yu H, Wu G, Tu X, Min J, Drozak J, Xu C. Structural insights into SETD3-mediated histidine methylation on β-actin. Elife. 2019 Feb; 8.

Gurel PS, Kim LY, Ruijgrok PV, Omabegho T, Bryant Z, Alushin GM. Cryo-EM structures reveal specialization at the myosin VI-actin interface and a mechanism of force sensitivity. eLife. 2017; 6(Md):1–33. doi: 10.7554/eLife.31125.

Hatano T, Sivashanmugam L, Suchenko A, Hussain H, Balasubramanian MK. Pick-ya actin – a method to purify actin isoforms with bespoke key post-translational modifications. Journal of Cell Science. 2020 01; 133(2):jcs241406. https://doi.org/10.1242/jcs.241406, doi: 10.1242/jcs.241406.

Helal MA, Khalifa S, Ahmed S. Differential Binding of Latrunculins to G-Actin: A Molecular Dynamics Study. Journal of Chemical Information and Modeling. 2013; 53(9):2369–2375. https://doi.org/10.1021/ci400317j, doi: 10.1021/ci400317j, pMID: 23988111.

Hocky GM, Baker JL, Bradley MJ, Sinitskiy AV, De La Cruz EM, Voth GA. Cations Stiffen Actin Filaments by Adhering a Key Structural Element to Adjacent Subunits. The Journal of Physical Chemistry B. 2016; 120(20):4558–4567. https://doi.org/10.1021/acs.jpcb.6b02741, doi: 10.1021/acs.jpcb.6b02741, pMID: 27146246.

Horan BG, Hall AR, Vavylonis D. Insights into Actin Polymerization and Nucleation Using a Coarse-Grained Model. Biophysical Journal. 2020; 119(3):553–566. https://www.sciencedirect.com/science/article/pii/S0006349520304951, doi: https://doi.org/10.1016/j.bpj.2020.06.019.

Humphrey W, Dalke A, Schulten K. VMD: Visual Molecular Dynamics. Journal of molecular graphics. 1996; 14(October 1995):33–38. https://www.tapbiosystems.com/tap/products/index.htm.

Jaffrelot Inizan T, Célerse F, Adjoua O, El Ahdab D, Jolly LH, Liu C, Ren P, Montes M, Lagarde N, Lagardère L, Monmarché P, Piquemal JP. High-resolution mining of the SARS-CoV-2 main protease conformational space: supercomputer-driven unsupervised adaptive sampling. Chemical Science. 2021; 12(2003). doi: 10.1039/d1sc00145k.

Jaswandkar SV, Faisal HMN, Katti KS, Katti DR. Dissociation Mechanisms of G-actin Subunits Govern Deformation Response of Actin Filament. Biomacromolecules. 2021; 22(2):907–917. https://doi.org/10.1021/acs.biomac.0c01602, doi: 10.1021/acs.biomac.0c01602, pMID: 33481563.

Jepsen L, Sept D. Effects of Nucleotide and End-Dependent Actin Conformations on Polymerization. Biophysical Journal. 2020; 119(9):1800–1810. https://www.sciencedirect.com/science/article/pii/S0006349520307359, doi: https://doi.org/10.1016/j.bpj.2020.09.024.

Jing Z, Liu C, Cheng SY, Qi R, Walker BD, Piquemal JP, Ren P. Polarizable Force Fields for Biomolecular Simulations: Recent Advances and Applications. Annual Review of Biophysics. 2019; 48(1):371–394. https://doi.org/10.1146/annurev-biophys-070317-033349, doi: 10.1146/annurev-biophys-070317-033349, pMID: 30916997.

Jing Z, Rackers JA, Pratt LR, Liu C, Rempe SB, Ren P. Thermodynamics of ion binding and occupancy in potassium channels. Chem Sci. 2021; 12:8920–8930. http://dx.doi.org/10.1039/D1SC01887F, doi: 10.1039/D1SC01887F.

Johnson P, Harris CI, Perry SV. 3-Methylhistidine in actin and other muscle proteins. Biochemical Journal. 1967 10; 105(1):361–370. https://doi.org/10.1042/bj1050361, doi: 10.1042/bj1050361.

Jégou A, Niedermayer T, Orbán J, Didry D, Lipowsky R, Carlier MF, Romet-Lemonne G. Individual Actin Filaments in a Microfluidic Flow Reveal the Mechanism of ATP Hydrolysis and Give Insight Into the Properties of Profilin. PLOS Biology. 2011 09; 9(9):1–10. https://doi.org/10.1371/journal.pbio.1001161, doi: 10.1371/journal.pbio.1001161.

Kadaoluwa Pathirannahalage SP, Meftahi N, Elbourne A, Weiss ACG, McConville CF, Padua A, Winkler DA, Costa Gomes M, Greaves TL, Le TC, Besford QA, Christofferson AJ. Systematic Comparison of the Structural and Dynamic Properties of Commonly Used Water Models for Molecular Dynamics Simulations. Journal of Chemical Information and Modeling. 2021; 61(9):4521–4536. https://doi.org/10.1021/acs.jcim.1c00794, doi: 10.1021/acs.jcim.1c00794, pMID: 34406000.

Kanematsu Y, Narita A, Oda T, Koike R, Ota M, Takano Y, Moritsugu K, Fujiwara I, Tanaka K, Komatsu H, Nagae T, Watanabe N, Iwasa M, Maéda Y, Takeda S. Structures and mechanisms of actin ATP hydrolysis. Proc Natl Acad Sci U S A. 2022 Oct; 119(43):e2122641119.

Kang H, Bradley MJ, McCullough BR, Pierre A, Grintsevich EE, Reisler E, Cruz EMDL. Identification of cation-binding sites on actin that drive polymerization and modulate bending stiffness. Proceedings of the National Academy of Sciences. 2012; 109(42):16923–16927. https://www.pnas.org/doi/abs/10.1073/pnas.1211078109, doi: 10.1073/pnas.1211078109.

Kapell S, Jakobsson ME. Large-scale identification of protein histidine methylation in human cells. NAR Genomics and Bioinformatics. 2021 05; 3(2):lqab045. https://doi.org/10.1093/nargab/lqab045, doi: 10.1093/nargab/lqab045.

Kim YC, Hummer G. Coarse-grained Models for Simulations of Multiprotein Complexes: Application to Ubiquitin Binding. Journal of Molecular Biology. 2008; 375(5):1416–1433. https://www.sciencedirect.com/science/article/pii/S0022283607015628, doi: https://doi.org/10.1016/j.jmb.2007.11.063.

Kopec W, Köpfer DA, Vickery ON, Bondarenko AS, Jansen TLC, de Groot BL, Zachariae U. Direct knock-on of desolvated ions governs strict ion selectivity in K+ channels. Nature Chemistry. 2018 Aug; 10(8):813–820. https://doi.org/10.1038/s41557-018-0105-9, doi: 10.1038/s41557-018-0105-9.

Kratochvil HT, Carr JK, Matulef K, Annen AW, Li H, Maj M, Ostmeyer J, Serrano AL, Raghuraman H, Moran SD, Skinner JL, Perozo E, Roux B, Valiyaveetil FI, Zanni MT. Instantaneous ion configurations in the K⁺ ion channel selectivity filter revealed by 2D IR spectroscopy. Science. 2016; 353(6303):1040–1044. https://www.science.org/doi/abs/10.1126/science.aag1447, doi: 10.1126/science.aag1447.

Kruth KA, Rubenstein PA. Two Deafness-causing (DFNA20/26) Actin Mutations Affect Arp2/3-dependent Actin Regulation*. Journal of Biological Chemistry. 2012; 287(32):27217–27226. https://www.sciencedirect.com/science/article/pii/S0021925820479190, doi: https://doi.org/10.1074/jbc.M112.377283.

Kwiatkowski S, Drozak J. Protein Histidine Methylation. Curr Protein Pept Sci. 2020; 21(7):675–689.

Kwiatkowski S, Seliga AK, Vertommen D, Terreri M, Ishikawa T, Grabowska I, Tiebe M, Teleman AA, Jagielski AK, Veiga-Da-Cunha M, Drozak J. SETD3 protein is the actin-specific histidine N-methyltransferase. eLife. 2018; 7(2016):1–42. doi: 10.7554/eLife.37921.

Lagardère L, Aviat F, Piquemal JP. Pushing the Limits of Multiple-Time-Step Strategies for Polarizable Point Dipole Molecular Dynamics. Journal of Physical Chemistry Letters. 2019; 10(10):2593–2599. doi: 10.1021/acs.jpclett.9b00901.

Lappalainen P, Kotila T, Jégou A, Romet-Lemonne G. Biochemical and mechanical regulation of actin dynamics. Nat Rev Mol Cell Biol. 2022 Aug; 23.

Laurent B, Chavent M, Cragnolini T, Dahl ACE, Pasquali S, Derreumaux P, Sansom MSP, Baaden M. Epock: Rapid analysis of protein pocket dynamics. Bioinformatics. 2015; 31(9):1478–1480. doi: 10.1093/bioinformatics/btu822.

Li H, Ngo V, Silva MCD, Salahub DR, Callahan K, Roux B, Noskov SY. Representation of Ion–Protein Interactions Using the Drude Polarizable Force-Field. The Journal of Physical Chemistry B. 2015; 119(29):9401–9416. doi: 10.1021/jp510560k.

Lynch CI, Klesse G, Rao S, Tucker SJ, Sansom MSP. Water Nanoconfined in a Hydrophobic Pore: Molecular Dynamics Simulations of Transmembrane Protein 175 and the Influence of Water Models. ACS Nano. 2021; 15(12):19098–19108. https://doi.org/10.1021/acsnano.1c06443, doi: 10.1021/acsnano.1c06443, pMID: 34784172.

Ma W, You S, Regnier M, McCammon JA. Integrating comparative modeling and accelerated simulations reveals conformational and energetic basis of actomyosin force generation. Proceedings of the National Academy of Sciences. 2023; 120(9):e2215836120. https://www.pnas.org/doi/abs/10.1073/pnas.2215836120, doi: 10.1073/pnas.2215836120.

Mahmood SR, Xie X, Hosny El Said N, Venit T, Gunsalus KC, Percipalle P. β-actin dependent chromatin remodeling mediates compartment level changes in 3D genome architecture. Nature Communications. 2021 Sep; 12(1):5240. https://doi.org/10.1038/s41467-021-25596-2, doi: 10.1038/s41467-021-25596-2.

Maier JA, Martinez C, Kasavajhala K, Wickstrom L, Hauser KE, Simmerling C. ff14SB: Improving the Accuracy of Protein Side Chain and Backbone Parameters from ff99SB. Journal of Chemical Theory and Computation. 2015; 11(8):3696–3713. https://doi.org/10.1021/acs.jctc.5b00255, doi: 10.1021/acs.jctc.5b00255, pMID: 26574453.

McCullagh M, Saunders MG, Voth GA. Unraveling the Mystery of ATP Hydrolysis in Actin Filaments. Journal of the American Chemical Society. 2014; 136(37):13053–13058. https://doi.org/10.1021/ja507169f, doi: 10.1021/ja507169f, pMID: 25181471.

McGibbon RT, Beauchamp KA, Harrigan MP, Klein C, Swails JM, Hernández CX, Schwantes CR, Wang LP, Lane TJ, Pande VS. MDTraj: A Modern Open Library for the Analysis of Molecular Dynamics Trajectories. Biophysical Journal. 2015; 109(8):1528–1532. doi: 10.1016/j.bpj.2015.08.015.

Melcr J, Piquemal JP. Accurate Biomolecular Simulations Account for Electronic Polarization. Frontiers in Molecular Biosciences. 2019; 6. https://www.frontiersin.org/articles/10.3389/fmolb.2019.00143, doi: 10.3389/fmolb.2019.00143.

Melo MCR, Bernardi RC, De La Fuente-Nunez C, Luthey-Schulten Z. Generalized correlation-based dynamical network analysis: A new high-performance approach for identifying allosteric communications in molecular dynamics trajectories. Journal of Chemical Physics. 2020; 153(13). https://doi.org/10.1063/5.0018980, doi: 10.1063/5.0018980.

Merino F, Pospich S, Raunser S. Towards a structural understanding of the remodeling of the actin cytoskeleton. Seminars in Cell & Developmental Biology. 2020; 102:51–64. https://www.sciencedirect.com/science/article/pii/S1084952119301909, doi: https://doi.org/10.1016/j.semcdb.2019.11.018.

Miao Y, Feher VA, McCammon JA. Gaussian Accelerated Molecular Dynamics: Unconstrained Enhanced Sampling and Free Energy Calculation. Journal of Chemical Theory and Computation. 2015; 11(8):3584–3595. https://doi.org/10.1021/acs.jctc.5b00436, doi: 10.1021/acs.jctc.5b00436, pMID: 26300708.

Nietmann P, Kaub K, Suchenko A, Stenz S, Warnecke C, Balasubramanian MK, Janshoff A. Cytosolic actin isoforms form networks with different rheological properties that indicate specific biological function. Nature Communications. 2023 Dec; 14(1):7989. https://doi.org/10.1038/s41467-023-43653-w, doi: 10.1038/s41467-023-43653-w.

Nyman T, Schüler H, Korenbaum E, Schutt CE, Karlsson R, Lindberg U. The role of MeH73 in actin polymerization and ATP hydrolysis. Journal of Molecular Biology. 2002; 317(4):577–589. https://www.sciencedirect.com/science/article/pii/S0022283602954367, doi: https://doi.org/10.1006/jmbi.2002.5436.

Oda T, Iwasa M, Aihara T, Maéda Y, Narita A. The nature of the globular- to fibrous-actin transition. Nature. 2009 Jan; 457(7228):441–445. https://doi.org/10.1038/nature07685, doi: 10.1038/nature07685.

Okazaki Ki, Hummer G. Phosphate release coupled to rotary motion of F1-ATPase. Proceedings of the National Academy of Sciences. 2013; 110(41):16468–16473. doi: 10.1073/pnas.1305497110.

Olsson MHM, SØndergaard CR, Rostkowski M, Jensen JH. PROPKA3: Consistent treatment of internal and surface residues in empirical p K a predictions. Journal of Chemical Theory and Computation. 2011; 7(2):525–537. doi: 10.1021/ct100578z.

Oosterheert W, Blanc FEC, Roy A, Belyy A, Sanders MB, Hofnagel O, Hummer G, Bieling P, Raunser S. Molecular mechanisms of inorganic-phosphate release from the core and barbed end of actin filaments. Nature Structural & Molecular Biology. 2023 Sep; 30. https://doi.org/10.1038/s41594-023-01101-9, doi: 10.1038/s41594-023-01101-9.

Otterbein LR, Graceffa P, Dominguez R. The crystal structure of uncomplexed actin in the ADP state. Science. 2001; 293(5530):708–711. doi: 10.1126/science.1059700.

Pedregosa F, Varoquaux G, Gramfort A, Michel V, Thirion B, Grisel O, Blondel M, Prettenhofer P, Weiss R, Dubourg V, Vanderplas J, Passos A, Cournapeau D, Brucher M, Perrot M, Duchesnay E. Scikit-learn: Machine Learning in Python. JMLR. 2011; 12(82):2825–2830.

Perrin BJ, Ervasti JM. The actin gene family: Function follows isoform. Cytoskeleton. 2010; 67(10):630–634. doi: 10.1002/cm.20475.

Rackers JA, Wang Z, Lu C, Laury ML, Lagardère L, Schnieders MJ, Piquemal JP, Ren P, Ponder JW. Tinker 8: Software Tools for Molecular Design. Journal of Chemical Theory and Computation. 2018; 14(10):5273–5289. doi: 10.1021/acs.jctc.8b00529.

Rennebaum S, Caflisch A. Inhibition of interdomain motion in g-actin by the natural product latrunculin: A molecular dynamics study. Proteins: Structure, Function, and Bioinformatics. 2012; 80(8):1998–2008. https://onlinelibrary.wiley.com/doi/abs/10.1002/prot.24088, doi: https://doi.org/10.1002/prot.24088.

Reynolds MJ, Hachicho C, Carl AG, Gong R, Alushin GM. Bending forces and nucleotide state jointly regulate F-actin structure. Nature. 2022; 611:380–386. doi: 10.1038/s41586-022-05366-w.

Rubenstein PA, Wen KK. Insights into the effects of disease-causing mutations in human actins. Cytoskeleton. 2014; 71(4):211–229. https://onlinelibrary.wiley.com/doi/abs/10.1002/cm.21169, doi: https://doi.org/10.1002/cm.21169.

Šali A, Blundell TL, Comparative Protein Modelling by Satisfaction of Spatial Restraints; 1993.

Saunders MG, Tempkin J, Weare J, Dinner AR, Roux B, Voth GA. Nucleotide regulation of the structure and dynamics of G-actin. Biophysical Journal. 2014; 106(8):1710–1720. doi: 10.1016/j.bpj.2014.03.012.

Saunders MG, Voth GA. Water molecules in the nucleotide binding cleft of actin: Effects on subunit conformation and implications for ATP hydrolysis. Journal of Molecular Biology. 2011; 413(1):279–291. http://dx.doi.org/10.1016/j.jmb.2011.07.068, doi: 10.1016/j.jmb.2011.07.068.

Schroer CFE, Baldauf L, van Buren L, Wassenaar TA, Melo MN, Koenderink GH, Marrink SJ. Charge-dependent interactions of monomeric and filamentous actin with lipid bilayers. Proceedings of the National Academy of Sciences. 2020; 117(11):5861–5872. https://www.pnas.org/doi/abs/10.1073/pnas.1914884117, doi: 10.1073/pnas.1914884117.

Shamloo A, Mehrafrooz B. Nanomechanics of actin filament: A molecular dynamics simulation. Cytoskeleton. 2018; 75(3):118–130. https://onlinelibrary.wiley.com/doi/abs/10.1002/cm.21429, doi: https://doi.org/10.1002/cm.21429.

Shi Y, Ren P, Schnieders M, Piquemal JP. 2. In: Polarizable Force Fields for Biomolecular Modeling John Wiley & Sons, Ltd; 2015. p. 51–86. https://onlinelibrary.wiley.com/doi/abs/10.1002/9781118889886.ch2, doi: https://doi.org/10.1002/9781118889886.ch2.

Shi Y, Xia Z, Zhang J, Best R, Wu C, Ponder JW, Ren P. Polarizable atomic multipole-based AMOEBA force field for proteins. Journal of Chemical Theory and Computation. 2013; 9(9):4046–4063. doi: 10.1021/ct4003702.

Song C, Weichbrodt C, Salnikov ES, Dynowski M, Forsberg BO, Bechinger B, Steinem C, de Groot BL, Zachariae U, Zeth K. Crystal structure and functional mechanism of a human antimicrobial membrane channel. Proceedings of the National Academy of Sciences. 2013; 110(12):4586–4591. https://www.pnas.org/doi/abs/10.1073/pnas.1214739110, doi: 10.1073/pnas.1214739110.

Souza PCT, Alessandri R, Barnoud J, Thallmair S, Faustino I, Grünewald F, Patmanidis I, Abdizadeh H, Bruininks BMH, Wassenaar TA, Kroon PC, Melcr J, Nieto V, Corradi V, Khan HM, Domański J, Javanainen M, Martinez-Seara H, Reuter N, Best RB, et al. Martini 3: a general purpose force field for coarse-grained molecular dynamics. Nature Methods. 2021 Apr; 18(4):382–388. https://doi.org/10.1038/s41592-021-01098-3, doi: 10.1038/s41592-021-01098-3.

Splettstoesser T, Holmes KC, Noé F, Smith JC. Structural modeling and molecular dynamics simulation of the actin filament. Proteins: Structure, Function, and Bioinformatics. 2011; 79(7):2033–2043. https://onlinelibrary.wiley.com/doi/abs/10.1002/prot.23017, doi: https://doi.org/10.1002/prot.23017.

Splettstoesser T, Noé F, Oda T, Smith JC. Nucleotide-dependence of G-actin conformation from multiple molecular dynamics simulations and observation of a putatively polymerization-competent superclosed state. Proteins: Structure, Function, and Bioinformatics. 2009; 76(2):353–364. https://onlinelibrary.wiley.com/doi/abs/10.1002/prot.22350, doi: https://doi.org/10.1002/prot.22350.

Stone AJ. Distributed multipole analysis, or how to describe a molecular charge distribution. Chemical Physics Letters. 1981; 83(2):233–239. doi: 10.1016/0009-2614(81)85452-8.

Svitkina T. The Actin Cytoskeleton and Actin-Based Motility. Cold Spring Harbor Perspectives in Biology. 2018; 10(1):a018267. doi: 10.1101/cshperspect.a018267.

Vanommeslaeghe K, Hatcher E, Acharya C, Kundu S, Zhong S, Shim J, Darian E, Guvench O, Lopes P, Vorobyov I, Mackerell Jr AD. CHARMM general force field: A force field for drug-like molecules compatible with the CHARMM all-atom additive biological force fields. Journal of Computational Chemistry. 2010; 31(4):671–690. https://onlinelibrary.wiley.com/doi/abs/10.1002/jcc.21367, doi: https://doi.org/10.1002/jcc.21367.

Varland S, Vandekerckhove J, Drazic A. Actin Post-translational Modifications: The Cinderella of Cytoskeletal Control. Trends in Biochemical Sciences. 2019; 44(6):502–516. https://doi.org/10.1016/j.tibs.2018.11.010, doi: 10.1016/j.tibs.2018.11.010.

Virtanen P, Gommers R, Oliphant TE, Haberland M, Reddy T, Cournapeau D, Burovski E, Peterson P, Weckesser W, Bright J, van der Walt SJ, Brett M, Wilson J, Millman KJ, Mayorov N, Nelson ARJ, Jones E, Kern R, Larson E, Carey CJ, et al. SciPy 1.0: fundamental algorithms for scientific computing in Python. Nature Methods. 2020; 17(3):261–272. doi: 10.1038/s41592-019-0686-2.

Walker B, Jing Z, Ren P. Molecular dynamics free energy simulations of ATP:Mg2+ and ADP:Mg2+ using the polarisable force field AMOEBA. Molecular Simulation. 2020; 0(0):1–10. https://doi.org/10.1080/08927022.2020.1725003, doi: 10.1080/08927022.2020.1725003.

Wegner A. Treadmilling of actin at physiological salt concentrations: An analysis of the critical concentrations of actin filaments. Journal of Molecular Biology. 1982; 161(4):607–615. https://www.sciencedirect.com/science/article/pii/0022283682904119, doi: https://doi.org/10.1016/0022-2836(82)90411-9.

Welford BP. Note on a Method for Calculating Corrected Sums of Squares and Products. Technometrics. 1962; 4(3):419–420. https://www.tandfonline.com/doi/abs/10.1080/00401706.1962.10490022, doi: 10.1080/00401706.1962.10490022.

Westerlund AM, Fleetwood O, Pérez-Conesa S, Delemotte L. Network analysis reveals how lipids and other cofactors influence membrane protein allostery. J Chem Phys. 2020 Oct; 153(14):141103.

Wilkinson AW, Diep J, Dai S, Liu S, Ooi YS, Song D, Li TM, Horton JR, Zhang X, Liu C, Trivedi DV, Ruppel KM, Vilches-Moure JG, Casey KM, Mak J, Cowan T, Elias JE, Nagamine CM, Spudich JA, Cheng X, et al. SETD3 is an actin histidine methyltransferase that prevents primary dystocia. Nature. 2019; 565(7739):372–376. http://dx.doi.org/10.1038/s41586-018-0821-8, doi: 10.1038/s41586-018-0821-8.

Wioland H, Guichard B, Senju Y, Myram S, Lappalainen P, Jégou A, Romet-Lemonne G. ADF/Cofilin Accelerates Actin Dynamics by Severing Filaments and Promoting Their Depolymerization at Both Ends. Curr Biol. 2017 Jul; 27(13):1956–1967.e7.

Wioland H, Jegou A, Romet-Lemonne G. Torsional stress generated by ADF/cofilin on cross-linked actin filaments boosts their severing. Proceedings of the National Academy of Sciences. 2019; 116(7):2595–2602. https://www.pnas.org/doi/abs/10.1073/pnas.1812053116, doi: 10.1073/pnas.1812053116.

Zhang C, Lu C, Jing Z, Wu C, Piquemal JP, Ponder JW, Ren P. AMOEBA Polarizable Atomic Multipole Force Field for Nucleic Acids. Journal of Chemical Theory and Computation. 2018; 14(4):2084–2108. https://doi.org/10.1021/acs.jctc.7b01169, doi: 10.1021/acs.jctc.7b01169, pMID: 29438622.

Zsolnay V, Katkar HH, Chou SZ, Pollard TD, Voth GA. Structural basis for polarized elongation of actin filaments. Proceedings of the National Academy of Sciences of the United States of America. 2020; 117(48):30458–30464. doi: 10.1073/pnas.2011128117.

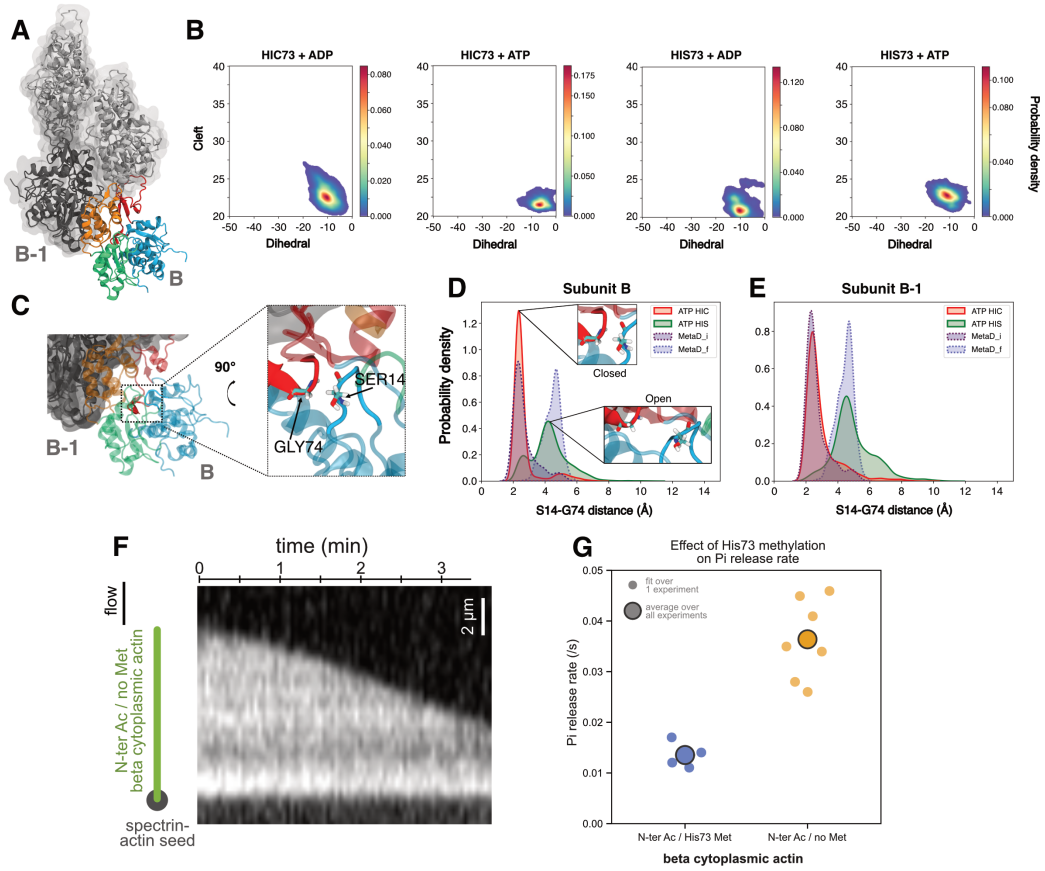

Figure 5. Actin flexibility at the barbed end and inorganic phosphate release. A- Representation of ultimate (subunit B, colored by subdomains as presented in figure 1-A) and penultimate (subunit B-1, dark grey) at the filament barbed end. **B-** Distribution of Cleft-Dihedrals angles for ultimate (B) subunit in HIC73 and HIS73 systems containing either ADP or ATP molecules. Distributions for the B-1 subunit are presented in Figure S8. Differences of cleft and dihedral values observed are all significant expect for the dihedral values in between HIS73+ATP and HIS73+ADP systems (Table S3). **C-** Zoom on the G74-S14 backdoor in the ultimate subunit. **D-** Distribution of distances between G74 and S14 residues in HIS73+ATP and HIC73+ATP states of B subunit. **E-** Distribution of distances between G74 and S14 residues in HIS73+ATP and HIC73+ATP states of B-1 subunit. The metaD_i (purple) and metaD_f (blue) distributions correspond respectively to distances observed in the initial and final states of metadynamics simulations extracted from ref ***Oosterheert et al.*** (***2023***) (see Method). In this simulation the G74-S14 backdoor is closed in the first half of the simulation(metaD_i, purple dashed curve), and open in the second half of the simulation (metaD_f blue dashed curve). **F-** Sketch of the actin filament depolymerization assay performed in microfluidics on left. β-actin filaments elongated from glass-anchored spectrin-actin seeds in FME buffer, are exposed to buffer only to induce their depolymerization (see Methods). On right, kymograph of a single actin filament observed in epifluorescence during depolymerization. **G-** Pi release rates measured experimentally for HIC73 or HIS73 β-actin filaments. Individual data points represent the fitted value of the Pi release rate, for at least 30 filaments per condition. Large data points are the mean values of those repeated experiments. T-test p-value = 1.1 10^{-4}.